Exp Fluids (2011) 50:1651–1657
DOI 10.1007/s00348-010-1028-4

RESEARCH ARTICLE

Visualizing supersonic inlet duct unstart using planar laser Rayleigh scattering

Hyungrok Do · Seong-kyun Im · M. Godfrey Mungal · Mark A. Cappelli

Received: 2 April 2010 / Revised: 13 November 2010 / Accepted: 10 December 2010 / Published online: 24 December 2010

Abstract Planar laser Rayleigh scattering (PLRS) from condensed CO_2 particles is used to visualize flow structure in a Mach 5 wind tunnel undergoing unstart. Detailed flow features such as laminar/turbulent boundary layers and shockwaves are readily illustrated by the technique. A downstream transverse air jet, inducing flow unchoking downstream of the jet, is injected into the free stream flow of the tunnel, resulting in tunnel unstart. Time sequential PLRS images reveal that the boundary layer growth/separation on a surface with a thick turbulent boundary layer, initiated by the jet injection, propagates upstream and produces an oblique unstart shock. The tunnel unstarts upon the arrival of the shock at the inlet. In contrast, earlier flow separation on the opposite surface, initially supporting a thin laminar boundary layer, is observed when a jet induced bow shock strikes that surface. The resulting disturbance to this boundary layer also propagates upstream and precedes the formation of an unstart shock.

1 Introduction

Several studies have addressed the mechanism associated with scramjet engine unstart which can cause in-flight engine malfunctioning (Wieting 1976; Hawkins and Marquart 1995; Rodi et al. 1996; Shimura et al. 1998; O'Byrne et al. 2000; Wagner et al. 2008, 2009a, b). Unstart is believed to be caused by the thermal choking (Mashio et al. 2001) of the supersonic flow triggered by increased heat release in the combustor as a result of an increase in fuel injection, leading to an abrupt loss of thrust (Heiser and Pratt 1993; Sato et al. 1997; Kodera et al. 2003). Simulations (McDaniel and Edwards 2001) indicate that the pressure rise resulting from the heat release (thermal choking) is followed by boundary layer separation cascading into large-scale disturbances and blockage of the upstream flow. To delay this unstart transition, researchers have proposed the use of isolators (Curran et al. 1996; Sato et al. 1997; Wang and Le 2000; Tam et al. 2008), boundary layer bleeding (Kodera et al. 2003), and vortex generator jets (Valdivia et al. 2009). The unstart dynamics also results in the spawning of an unstart shock system induced by this boundary layer separation that propagates upstream. The propagation speed of this unstart shock was estimated to be in the range of 10–27 m/s (Wieting 1976) and in some cases as high as 55–70 m/s (Rodi et al. 1996), as determined by wall pressure measurements.

There are relatively few experimental studies of combustor-driven unstart dynamics due to the difficulties in providing realistic flight conditions (high enthalpy supersonic flows) in ground test facilities. Some insight into the unstart process can be obtained in facilities that at least partially reproduce flight conditions (comparable Mach number and pressure, but lower static temperature). In a very recent study, Wagner et al. (2008, 2009a, b) investigated flow unstart that was caused by the downstream mechanical actuation of a plate, which partially blocked the flow at the exit of the supersonic tunnel. In that study, high-speed Schlieren photography and particle image velocimetry (PIV) were used to characterize unstart dynamics. While providing good visualization, Schlieren is a line-of-sight measurement. On the other hand, PIV provides planar

H. Do (✉) · S. Im · M. G. Mungal · M. A. Cappelli
Mechanical Engineering Department, Stanford University, Stanford, CA 94305-3032, USA
e-mail: hyungrok@stanford.edu

M. G. Mungal
School of Engineering, Santa Clara University, Santa Clara, CA 95053, USA

information, but is by its very nature, pixelated to provide reasonable velocity statistics. While both diagnostics are very useful in providing information about general flow features, a better (albeit qualitative) visualization technique can be found for resolving fine-scale features in the flow.

In this paper, we visualized in more detail supersonic unstart flow features (e.g. boundary layer structure, shockwave interactions) using Rayleigh scattering from condensed CO_2 particles (particulate fog). Miles and Lempert (1997), Wu et al. (2000), and Poggie et al. (2004) have demonstrated the general use of this diagnostic technique for low-temperature/pressure supersonic flows expanded through the converging/diverging nozzle of a supersonic wind tunnel of low (ambient) stagnation temperature. The expanding nozzle flow experiences a drop in static temperature, and when seeded with CO_2 vapor, produces condensed (solid) CO_2 particles. These CO_2 particles subsequently evaporate under varying environments provided by primary flow features such as shockwaves and boundary layers where the local static temperature increases. Laser light scattered from the particles, typically several nanometers to tens of nanometers in size, highlight these features with enough contrast allowing a high-fidelity visualization of the flow. However, this visualization technique is constrained to flow conditions that are distributed across the CO_2 sublimation curve, usually over a fairly low temperature regime (<150 K) at less than atmospheric pressure. For the present study, an in-draft Ma = 5 supersonic wind tunnel (see below), utilizing a vacuum tank, at modest static pressures (1 kPa) and ambient static temperature (50 K) accesses this regime for flow visualization. As described below, the unstart of the supersonic flow induced by the injection of a downstream air jet generates features that are easily discerned by Rayleigh scattering from this CO_2 fog. The images of the detailed flow features, taken sequentially with a time resolution of less than a millisecond, provide an improved description of the behavior of the unstart shock, the possible role of boundary layers in the unstart process, and the propagation of flow separation that depends on initial boundary layer conditions, e.g. thin laminar boundary layers on the splitter plate and thick turbulent boundary layers on the tunnel walls.

2 Experimental setup

The experimental facility consists of a Ma = 5 in-draft wind tunnel, an integrated laser system and a jet injection module.

A schematic of the Ma = 5 wind tunnel is shown in Fig. 1. High-pressure air (p_0 = 350 kPa and T_0 = 300 K) containing CO_2 (approximately 25% by volume) expands

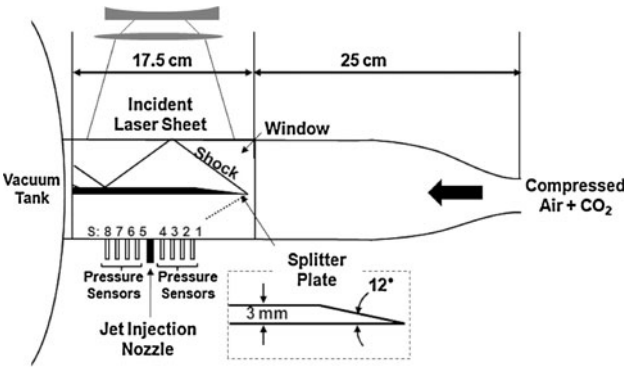

Fig. 1 A schematic of the experimental setup

through a converging/diverging nozzle (25:1 area ratio) to establish a relatively uniform Ma = 5 flow in a rectangular test section (4 cm × 4 cm cross-sectional area). The exit of the tunnel is connected to a vacuum tank that accommodates the incoming mass flow for approximately 5 s of run time. During this run time, the vacuum tank pressure is maintained at values lower than the static pressure in the test section. A honeycomb of 2.5 cm in length and 3 mm hexagonal cells is placed upstream of the converging/diverging nozzle to suppress flow swirling, mostly generated at various junctions in the gas stream inlet piping. The static pressure and temperature of the flow in the test section are approximately 1 kPa and 50 K, respectively.

A detailed characterization of the variation in Mach number of the flow across the test section is carried out by measuring the shock angle from a sharp leading wedge of 12° angle using Schlieren photography. The measured Mach number midway across the tunnel is approximately Ma = 4.9, with a 5% variation wall to wall (boundary layers were not resolved). Windows on both sides of the test section and transparent upper/lower walls allow optical access. A 3-mm-thick splitter plate (aluminum plate), having a sharp leading wedge and a transparent slot of an embedded acrylic plate, divides the test section into two parts of equal cross-sectional area. The sharp leading wedge of an asymmetric design (12° angled wedge in the top half of channel), as shown in Fig. 1, is used to generate a relatively shock-free flow in the lower half while it causes a series of shock reflections in the upper half. Static pressure traces on the bottom wall of the tunnel are recorded using eight fast response (100 kHz) pressure sensors (S1–S8: PCB Piezotronics, Model 113A26). The sensors and the jet injection nozzle, placed between S4 and S5, are separated by 15 mm along the centerline of the bottom wall parallel to the free stream flow direction: S1 and S8 are located 60 mm upstream and downstream from the nozzle, respectively. The distance between the tip of the splitter plate (270 mm downstream from the converging/diverging nozzle throat) and the nozzle is 75 mm.

The experimental components for Rayleigh scattering include a Nd:YAG laser (New Wave, Gemini PIV) capable of generating approximately 100 mJ/pulse (532 nm wavelength) energy with 10 Hz pulse repetition, an unintensified CCD camera (La Vision, Imager Intense), and a computer (not shown) to facilitate data acquisition. The laser beam is transformed into a thin sheet of 0.5 mm thickness to illuminate the test section using a combination of two concave cylindrical lenses and a convex spherical lens. Scattered light is captured by the camera along a direction normal to the laser sheet. Laser firing is synchronized with the CCD camera exposure (3-μs shutter), as illustrated in Fig. 2. One of the laser pulses is selected to trigger the jet injection module while the tunnel is operating, but delayed as desired by a pulse delay generator (SRS, DG 535) to take time sequential images at different phases (Δt following the injection of the jet) in the flow evolution induced by the jet injection. The jet injection is controlled by a solenoid valve (ASCO, Red Hat II) driven by a controller (Optimal Engineering System Inc.) receiving the trigger signal from the delay generator. A sonic jet (air, in these studies presented here) is injected into the test section through a 3-mm-diameter hole in the bottom wall resulting in a flow disturbance

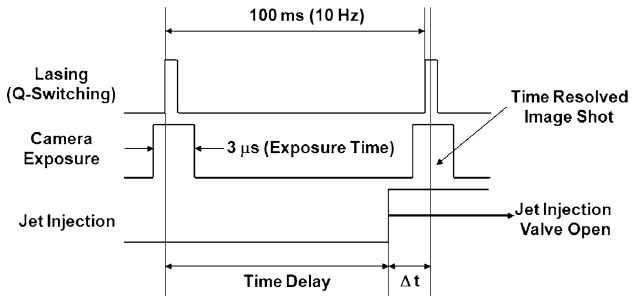

Fig. 2 A time table of the signals for taking an image at Δt after the jet injection

and an overall increase in flow pressure and temperature. Relevant to the jet interaction and mixing with the supersonic free stream is the square root of the ratio of the jet momentum flux to that of the free stream, defined by:

$$R = \sqrt{\frac{(\rho u^2)_{jet}}{(\rho u^2)_{\infty}}} = \sqrt{\frac{(\gamma p M^2)_{jet}}{(\gamma p M^2)_{\infty}}}$$

Here, ρ, u, γ, p, and M are air density, velocity, ratio of specific heats, pressure, and Mach number of the jet (subscript *jet*) and free stream (subscript ∞) flow, respectively. For our results described here, R is approximately 4.5.

3 Results

3.1 Unstart

Tunnel unstart induced by air jet injection is clearly reflected in the pressure traces measured on the bottom surface of the wind tunnel. Figure 3a documents the sudden pressure rise at the various locations on the wall following the jet injection through the nozzle located between S4 and S5. The time reference (t = 0 s) in this figure corresponds to when the pressure first rises at the sensor located at S8 (i.e., the farthest downstream region characterized). The pressure at S8 starts to rise abruptly at approximately 10 ms after the jet injection trigger signal opens the solenoid valve. Absolute pressure offsets are subtracted from the traces to illustrate relative differences between the pressure recorded before and after the jet injection. The pressure traces recorded at the locations nearest to the jet nozzle (S4 and S5, not shown) fluctuate significantly, due to flow instabilities in the near field of the jet. It is noteworthy that the first pressure increase is recorded at S8 and this high-pressure region then expands

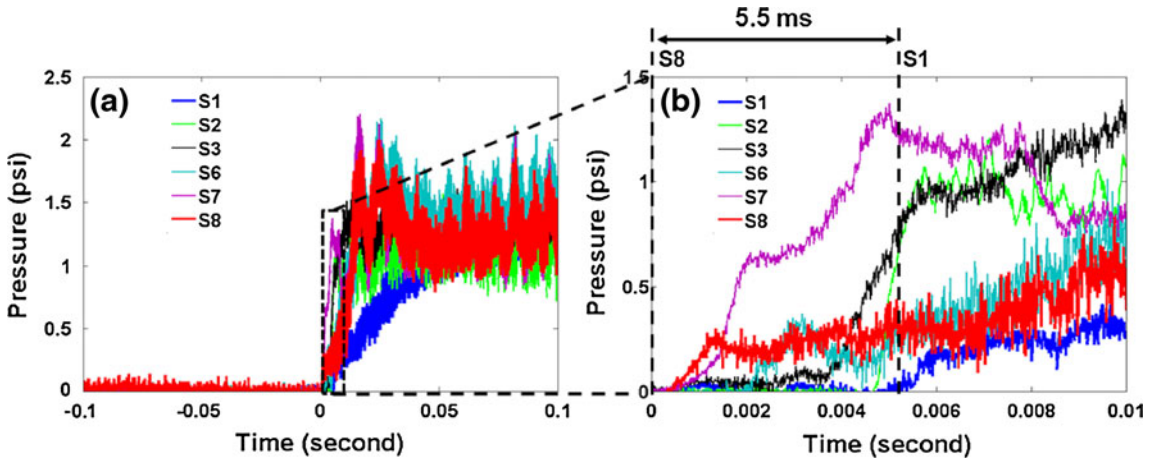

Fig. 3 Pressure traces recorded on the *bottom* wall of the wind tunnel: **a** pressure traces between 100 ms before and after the pressure rise at S8, and **b** an expanded scale (0–10 ms)

toward the upstream region of the tunnel, presumably along the subsonic boundary layer, in succession through to the location at S1 (an expanded scale is shown in Fig. 3b). This ordering in the rise in pressure confirms that unchoking originates downstream of the jet injection point, triggering tunnel unstart, i.e., a transition to a subsonic flow regime. We conjecture that the unchoked flow, i.e., the subsonic flow caused by the mass injection, first appears far downstream near the tunnel exit due to the reduced supersonic core flow area by the growth of boundary layers on the tunnel surfaces and the increment of mass flow rate by the jet injection. The propagation of this high-pressure region from S8 to S1 (over 12 cm distance) takes approximately 5.5 ± 0.5 ms (see Fig. 3b) indicating that that this pressure wave propagates at a speed of approximately 22 ± 2 m/s (a mean of 4 measurements). For comparison, the free stream speed is approximately 750 m/s.

3.2 Flow visualization

The flow features in the test section are visualized by two-dimensional Rayleigh laser scattering signals from condensed CO_2. The generated fog predominantly occupies the core flow, since the condensed particles will sublimate in the hotter boundary layers. Some particles survive the large-scale mixing in the turbulent boundary layers, revealing boundaries between turbulent eddies and the relative size of the larger turbulent scales. Figure 4 is a composite Rayleigh scattering depiction of the basic features of the supersonic flow generated in the wind tunnel near the splitter plate tip and further downstream. The oblique waves originating from the leading edge of the wedged splitter plate tip in both the upper and lower half of the test section are clearly discernible. The upper wave reflects from the top wall and is visible in both images. That in the lower half arises due to imperfections in the tip and/or slight misalignment of the splitter plate surface relative to the direction of the main flow and is presumed to be weaker than the upper wave and thus shows no significant reflection in the lower wall. The vertical triangular-shaped region near the tip at the entrance to the lower half of the tunnel is an artifact due to shadowing of the laser sheet from the opaque region near the sharp tip. The most interesting feature resolved in this image is the turbulent boundary layer appearing on both the upper and the lower surfaces of the tunnel, while the initial boundary layer developing on the surface of the splitter plate, presumed to be laminar, is not resolvable by the diagnostic. The thickness of the tunnel wall boundary layers in this axial location fluctuates between 2 and 3 mm, representing 10–15% of the tunnel height. The thickness of the boundary layer is estimated by measuring the thickness of the region in the vicinity of the surface that is free of laser scattering, due to the absence of condensed particles. This region must represent a region of elevated temperature, due to flow deceleration and associated temperature recovery, however, at this time, it is difficult to correlate this thickness to a quantitative measure based on direct velocity measurements, e.g., 99% free stream flow velocity. The boundary layers on the upper and lower walls immediately behind the incident shockwaves appear to be thinner due to the post-shock compression/expansion of the flow and will be more apparent in Fig. 5.

Figure 5 is a Rayleigh scattered image of the region of the splitter tip, 16 ms following the jet injection in the downstream region (75 mm from the splitter plate tip), and now reveals a much more complex flow, including the development of boundary layers, additional shockwaves, and a slip line. Among the various flow features seen here, two important flow characteristics are depicted in this image, namely the arrival of an unstart shock and the shock-boundary layer interactions on all but the top surface of the splitter plate. At this time, in the evolution of the flow, the unstart shock is located in front of a thick dark region (presumably separated flow region) on the bottom wall; the cause of the flow separation is not discernible due to the limitations in the visualization technique in the lower-speed and/or high-pressure/temperature region. This

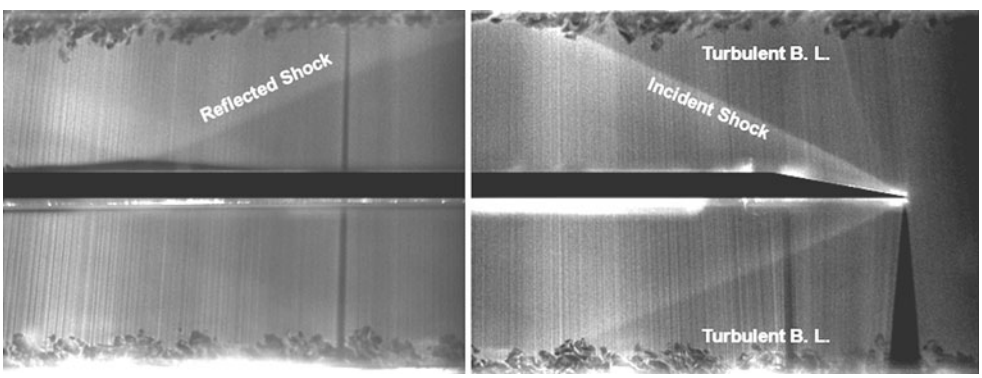

Fig. 4 An image of Rayleigh scattering from condensed CO_2 particles taken with a supersonic free stream flow

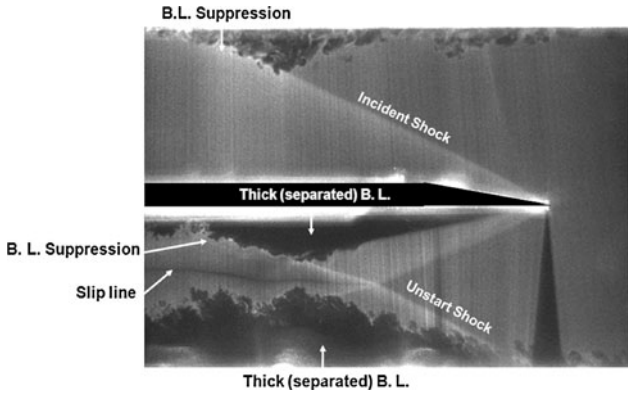

Fig. 5 Detailed flow features visualized by the scattered laser sheet

shock is initially induced by the jet injection and then propagates upstream (as will be shown in more detail below in Fig. 6). The core flow behind the unstart shock has different properties than that behind the now strengthened tip-generated shock, leading to the generation of a slip line that persists several channel heights downstream of the merging of the two shocks. Perhaps more pronounced than in Fig. 4, the strong shockwave-boundary layer interaction in the top half of the tunnel reveals strong boundary layer suppression, here, which implies boundary layer thinning. This boundary layer thinning due to the shockwave-boundary layer interaction has been observed experimentally (Wutson et al. 1969) and in a direct numerical simulation (DNS) (Pagella and Rist 2005) under relatively high Mach number conditions (Ma $\sim$ 6–10). Boundary layer thickening has been reported with lower Mach number flows [e.g. Ma $\sim$ 2.1 in the study of Humble et al. (2006)]. The interactions of the shocks and separated boundary layers are also observed on both the splitter plate and wall surfaces in the lower half. The unstart shock (refracted across the slip line) contacts the lower splitter plate surface while suppressing and reattaching the separated boundary layer.

3.3 Unstart time behavior

Time-synchronized Rayleigh scattering images of the flow evolution near the vicinity of the jet injection are shown in Fig. 6. Each image in Figs. 6 and 7 is taken with a separate tunnel run, triggered at a different time in the flow evolution. We observed quite reproducible sequences of the flow evolution with a jitter estimated to be much shorter than 0.5 ms, the minimum time difference between frames, under the present conditions. In the 12 ms image, the air jet is clearly entrained by the flow but not yet filling the tunnel, and the pressure disturbance (initially recorded at S8 at approximately 10 ms) propagating upstream in the wall boundary layer will have just arrived near the vicinity of

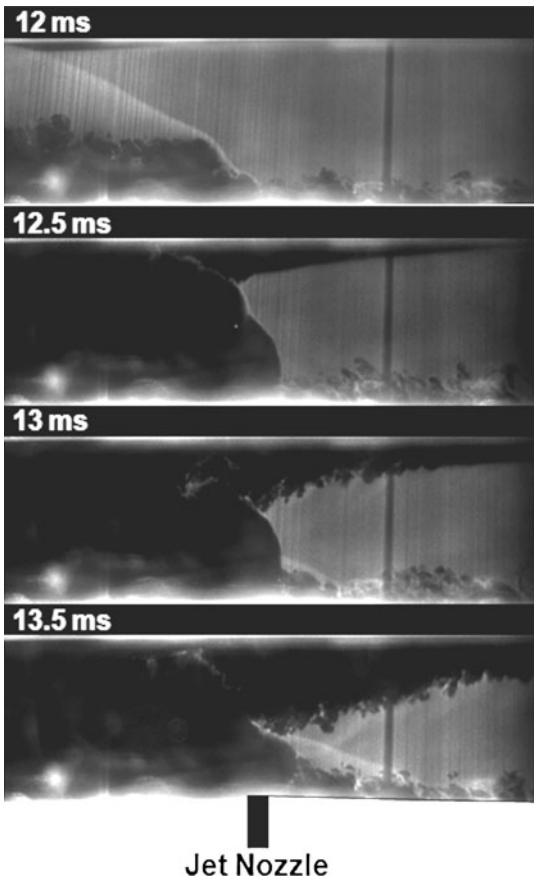

Fig. 6 A set of time sequential images taken in the region adjacent to the jet injection nozzle

the injection point. The bow shock generated by the jet strikes the upper surface inducing boundary layer thickening (separation) due to local compression [dark region on upper surface (i.e. lower surface of the splitter plate)]. In the subsequent frames (12.5–13.5 ms), the laminar boundary layer on the upper surface thickens (separated) while propagating upstream (presumably due to the propagation of pressure disturbances along the upper boundary layer) and eventually becomes turbulent. On the bottom wall, by 13 ms, we see the development of a turbulent boundary layer just upstream of the jet and bow shock and the formation of an unstart shock. By 13.5 ms, this unstart shock is well developed and begins to interact with the upper, growing boundary layer. As we will see in Fig. 7, the injected mass expands into the boundary layer region behind the unstart shock, driving the shock forward toward the inlet of the channel.

Time-synchronized Rayleigh scattering images of the flow evolution near the vicinity of the splitter plate tip are shown in Fig. 7. We see that by 13 ms, the boundary layer on the lower splitter plate surface has increased in thickness and generated a weak oblique shock. By 13.5 ms, this thickened (separated) boundary layer has reached the

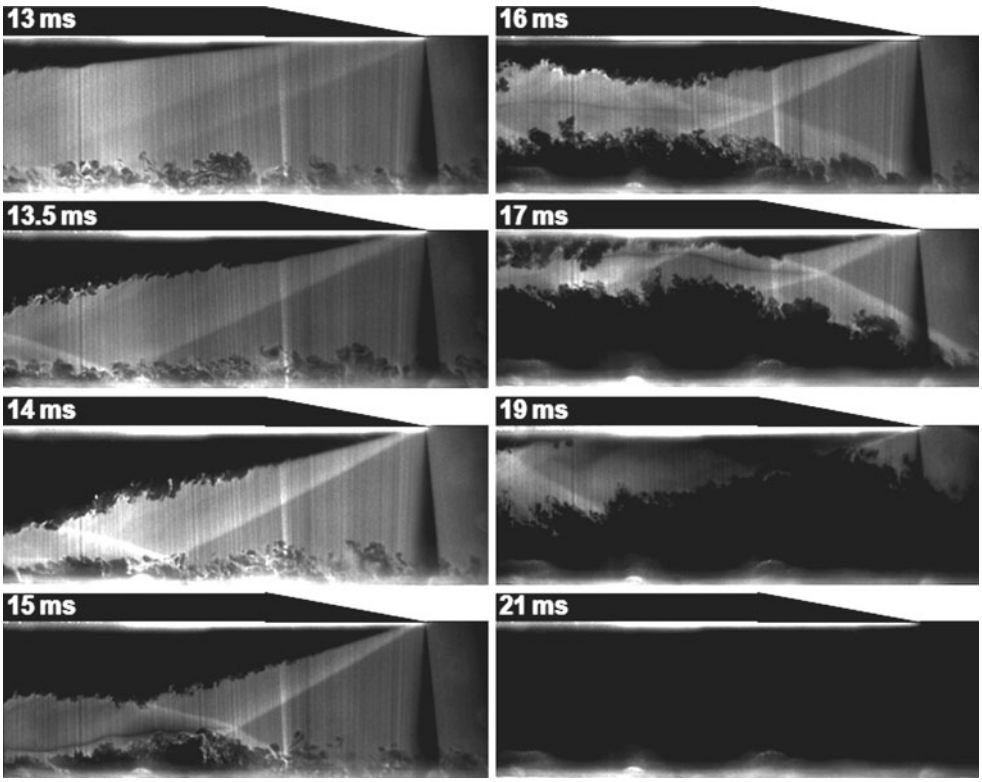

Fig. 7 A set of time sequential images depicting the time behavior of the unstart phenomenon in the region adjacent to the leading wedge of the splitter plate

splitter plate tip and the resulting shockwave appears stronger; the angle of the shock originating from the splitter plate tip is increased by 3° from ~23° to ~26° upon arrival of the thickened (separated) boundary layer at the tip (for reference, the Mach angle is approximately 12° under the current flow conditions). The lower unstart shock appears in this spatial window at 13.5 ms, and by comparing subsequential frames, appears to propagate upstream and is followed by the separated flow on the bottom wall. Again, as was seen in Fig. 5, the refracted unstart shock clearly suppresses boundary layer development on the surface of the splitter plate (during the time period between 15 and 17 ms). There may also be a slight suppression of the lower wall boundary layer due to interactions with the shock emanating from the splitter plate tip. At 19 ms, the unstart shock leaves the region of interest and the separated flow region on the bottom wall grows in extent to reach the splitter plate surface near the splitter plate leading edge. By 20 ms, the lower half of the tunnel is nearly completely unstarted and occupied by high pressure (presumably high temperature and subsonic) flow as evidenced by the complete absence of condensed CO_2 particles.

The speed of the unstart shock can be determined by the movement of the shock between frames captured at 13.5 and 16 ms. Under the conditions studied, the unstart shock propagates at approximately 15 ± 3 m/s. This speed is slower than that of the propagation of the wall pressure characterized by the wall pressure sensors, as shown in Fig. 3 (22 ± 2 m/s). The speed of the unstart shock appears to depend on the evolution of the separated flow on the lower wall as the region thickens. While it appears as though the two speeds are very different, we surmise that the thickening (separation) of the boundary layer and its movement, generating the unstart shock, is a consequence of the pressure wave that propagates upstream along the boundary layer.

4 Conclusions

An inlet duct unstart condition was generated in a $Ma = 5$ wind tunnel induced by downstream air injection. The sonic transverse air jet, injected into the free stream flow, is seen to cause a sudden rise in pressure and temperature downstream of the injection location. Surface pressures recorded on the bottom wall of the tunnel upstream and downstream of the injected jet indicate that the surface pressure initially rises at the furthest downstream sensor (S8), located 60 mm from the jet nozzle. This pressure disturbance propagates upstream to sensor S1, at 60 mm upstream from the jet nozzle over a time of 5.5 ms, corresponding to a speed of 22 m/s.

The detailed tunnel unstart process was studied by visualizing the supersonic flow using Rayleigh scattering of a thin laser sheet from condensed CO_2 particles in the free

stream flow. This diagnostic technique is capable of highlighting detailed flow features such as shockwaves, boundary layers, and slip lines. Turbulent boundary layers of 2–3 mm thickness on the upper and lower wall surfaces of the tunnel were seen before the jet injection. A thicker turbulent boundary layer evolved in front of the jet nozzle following jet injection, spawning an unstart shock which interacted with the initially laminar boundary layer on the splitter plate wall. This thickened (separated) boundary layer propagated upstream until it reached the leading tip of the splitter plate leading to a stronger shock emanating from the splitter plate tip. The interaction of this stationary shockwave with the unstart shock moving upstream, the continued forward propagation of the unstart shock, and the associated subsonic high pressure disturbance behind the turbulent boundary layer and the flow separation, which evolved on the bottom wall, eventually leads to a complete unstart of the flow.

Acknowledgments This work is sponsored by the Department of Energy sponsored Predictive Science Academic Alliance Program (PSAAP) at Stanford University. We thank Dr. Mirko Gamba for useful discussions.

References

Curran ET, Heiser WH, Pratt DT (1996) Fluid phenomena in scramjet combustion systems. Annu Rev Fluid Mech 28:323–360

Hawkins WR, Marquart EJ (1995) Two-dimensional generic inlet unstart detection at Mach 2.5–5.0. In: 6th international aerospace planes and hypersonics technologies conference, Chattanooga

Heiser WH, Pratt DT (1993) Hypersonic air breathing propulsion. In: AIAA education series, Washington

Humble RA, Scarano F, van Oudheusden BW (2006) Experimental study of an incident shock wave/turbulent boundary layer interaction using PIV. In: 36th AIAA fluid dynamics conference and exhibit, San Francisco

Kodera M, Tomioka S, Kanda T, Mitani T, Kobayashi K (2003) Mach 6 test of a scramjet engine with boundary-layer bleeding and two-staged fuel injection. In: 12th AIAA international space planes and hypersonic systems and technologies, Norfolk

Mashio S, Kurashina K, Bamba T, Okimoto S, Kaji S (2001) Unstart phenomenon due to thermal choke in scramjet module. In: AIAA/NAL-NASDA-ISAS 10th international space planes and hypersonic systems and technologies conference, Kyoto

McDaniel KS, Edwards JR (2001) Three-dimensional simulation of thermal choking in a model scramjet combustor. In: 39th aerospace sciences meeting and exhibit, Reno

Miles RB, Lempert WR (1997) Quantitative flow visualization in unseeded flows. Annu Rev Fluid Mech 29:285–326

O'Byrne S, Doolan M, Olsen SR, Houwing AFP (2000) Analysis of transient thermal choking processes in a model scramjet engine. J Propuls Power 16:808–814

Pagella A, Rist U (2005) Direct numerical simulations of shock-boundary layer interaction at Ma = 6. Comput Sci High Perform Comput 88:123–140

Poggie J, Erbland PJ, Smits AJ, Miles RB (2004) Quantitative visualization of compressible turbulent shear flows using condensate-enhanced Rayleigh scattering. Exp Fluids 37:438–454

Rodi PE, Emami S, Trexler CA (1996) Unsteady pressure behavior in a ramjet/scramjet inlet. J Propuls Power 12:486–493

Sato S, Izumikawa M, Tomioka S. Mitani T (1997) Scramjet engine test at Mach 6 flight condition. In: 33rd AIAA/ASME/SAE/ASEE joint propulsion conference and exhibit, Seattle

Shimura T, Mitani T, Sakuranaka N, Izumikawa M (1998) Load oscillations caused by unstart of hypersonic wind tunnels and engines. J Propuls Power 14:348–353

Tam C, Eklund D, Behdadnia R (2008) Influence of downstream boundary conditions on scramjet-isolator simulations. In: 26th AIAA applied aerodynamics conference, Honolulu

Valdivia A, Yuceil KB, Wagner JL, Clemens NT, Dolling DS (2009) Active control of supersonic inlet unstart using vortex generator jets. In: 39th fluid dynamics conference and exhibit, San Antonio

Wagner JL, Yuceil KB, Valdivia A, Clemens NT, Dolling DS (2008) PIV measurements of the unstart process in a supersonic inlet/isolator. In: 38th fluid dynamics conference and exhibit, Seattle

Wagner JL, Yuceil KB, Valdivia A, Clemens NT, Dolling DS (2009a) Experimental investigation of unstart in an inlet/isolator model in Mach 5 flow. AIAA J 47:1528–1542

Wagner JL, Yuceil KB, Clemens NT (2009b) PIV measurements of unstart of an inlet-isolator model in a Mach 5 flow. In: 39th fluid dynamics conference and exhibit, San Antonio

Wang X, Le J (2000) Computations of inlet/isolator for SCRAMjet engine. J Thermal Sci 9:334–338

Wieting AR (1976) Exploratory study of transient unstart phenomena in a three-dimensional fixed-geometry scramjet engine. NASA technical note: TN D-8156

Wu P, Lempert WR, Miles RB (2000) Megahertz pulse-burst laser and visualization of shock-wave/boundary-layer interaction. AIAA J 38:672–679

Wutson EC, Murphy JD, Rose WC (1969) Investigation of laminar and turbulent boundary layers interacting with externally generated shock waves. NASA technical note, NASA TN D-5512